Eur. Phys. J. C 9, 141–158 (1999)
DOI 10.1007/s100529900023

THE EUROPEAN PHYSICAL JOURNAL C

Scalar mesons and multichannel amplitudes

R. Kamiński[1], L. Leśniak[1], B. Loiseau[2]

[1] Department of Theoretical Physics, H. Niewodniczański Institute of Nuclear Physics, PL 31-342 Kraków, Poland
[2] LPTPE Université P. et M. Curie, 4, Place Jussieu, F-75252 Paris Cedex 05, France

Received: 19 October 1998 / Revised version: 25 January 1999 / Published online: 15 April 1999

Abstract. Properties of scalar–isoscalar mesons are analyzed in a unitary model using separable interactions in three decay channels: $\pi\pi$, $K\overline{K}$ and an effective $2\pi2\pi$. We obtain different solutions by fitting various data on the $\pi\pi$ and $K\overline{K}$ phase shifts and inelasticities including the CERN–Cracow–Munich measurements of the $\pi^- p_\uparrow \to \pi^+\pi^- n$ reaction on a polarized target. The analytical structure of the meson–meson multichannel amplitudes is studied with special emphasis on the role played by the S-matrix zeroes. S-matrix poles, located in the complex energy plane not too far from the physical region, are interpreted as scalar resonances. We see a wide $f_0(500)$, a narrow $f_0(980)$ and a relatively narrow $f_0(1400)$. In one of our solutions a resonance at about 1700 MeV is also found. Total, elastic and inelastic channel cross sections, branching ratios and coupling constants are evaluated and compared with available data. We construct an approximation to our model and show that the Breit–Wigner approach has a limited phenomenological applicability.

1 Introduction

A full classification and identification of the scalar mesons has not yet been well established [1]. Many theoretical and experimental efforts have recently been made for a better understanding of the scalar mesons as can be seen, for example, in the references given in [1,2]. From QCD one expects the presence of some scalar ($J^{PC} = 0^{++}, I = 0$) glueballs which can be mixed with ordinary $q\overline{q}$ scalar states [3]. The lowest scalar glueball masses predicted by lattice QCD calculations are in the range of 1500 MeV to 1700 MeV [4,5]. There are now lively discussions about the nature of the scalar mesons $f_0(1500)$ and $f_J(1710)$ and their possible mixture with scalar glueballs [4,6]. High-statistics experiments on meson production such as $p\overline{p}$ annihilation, πN scattering on unpolarized and polarized targets, central production in pp scattering, J/Ψ or other heavy meson decays and $\gamma\gamma$ collisions have been performed. Their analyses give some new evidence for the existence of five scalar–isoscalar mesons: $f_0(400–1200)$ or σ, $f_0(980)$, $f_0(1370)$, $f_0(1500)$ and $f_0(1710)$ [1].

In [7] we have analyzed new solutions for the scalar–isoscalar $\pi\pi$ phase shifts [8] together with previous $K\overline{K}$ results in the framework of a three coupled channel model based on an extension of the two-channel model of [9]. Separable potentials were used to describe interactions in the $\pi\pi$, and $K\overline{K}$ channels, and in an effective $2\pi2\pi$ channel. Let us recall that the use of separable potentials leads to an analytical solution for the S matrix which helps to check and understand the results. It furthermore represents one of the easiest ways to handle non-local interactions and so it should be adequate to describe, with a minimum number of parameters, the strong energy dependence in several coupled-channel reactions, as seems to be the case here. The simple analytical form of separable interactions is then phenomenologically very useful in fitting the $\pi\pi$ and $K\overline{K}$ experimental data from the corresponding thresholds up to 1.8 GeV.

The third effective $2\pi2\pi$ channel was introduced to take into account a strong four-pion production as observed in different experiments. In these data some evidence for four-pion clustering into a $\sigma\sigma$ pair, coming from a strong interaction between two pions, was found (see for example [10]). Our $2\pi2\pi$ effective channel, called $\sigma\sigma$, can, however, represent also other possible clusterings such as $\rho\rho$, $a_1(1260)\pi$, $\pi(1300)\pi$ and $\omega\omega$. One should not mix the effective threshold mass with twice the mass of the $f_0(500)$ or σ resonance which is seen in the $\pi\pi$ channel.

The parameters of the model were determined by a fit to two sets of $\pi\pi$ phase shifts and inelasticities obtained in a recent analysis of the CERN–Cracow–Munich measurements of the $\pi^- p_\uparrow \to \pi^+\pi^- n$ reaction on a *polarized* target [8]. It was stressed in [8] that the a_1 exchange gives an important contribution to the $\pi^- p \to \pi^+\pi^- n$ reaction amplitudes. Recently Achasov and Shestakov have also come to the conclusion that the a_1 exchange plays an important role in the reaction $\pi^- p \to \pi^0\pi^0 n$ on an unpolarized target [11]. This conclusion may be experimentally verified by *measurements on a polarized target*. The $\pi\pi$ data [8], covering the 600–1600 MeV $\pi\pi$ invariant mass range, were completed in the lower energy region by the $\pi\pi$ phase shifts of [12–14]. Further constraints were imposed by using the $K\overline{K}$ phase shifts from the $K\overline{K}$ threshold up to 1530 MeV [15].

We found a relatively narrow (90–180 MeV) scalar resonance $f_0(1400–1460)$. Our analysis of previous CERN–Munich unpolarized-target data [16] predicted a much broader ($\Gamma \approx 500$ MeV) state. We have also obtained a very wide ($\Gamma \approx 500$ MeV) $f_0(500)$ resonance and the well established narrow $f_0(980)$ ($\Gamma \approx 60$–70 MeV). Our model allows a theoretical study of the origin of the resonances by switching off the interchannel couplings. In all solutions found in [7] the $K\overline{K}$ interaction was repulsive or not attractive enough to create, by itself, a $K\overline{K}$ bound state.

In this paper we build two new solutions in which the $K\overline{K}$ state is bound in the uncoupled case. Our solutions are also characterized by the presence or absence of a $\sigma\sigma$ bound state. A gradual increase of the interchannel couplings allows one to link the S matrix poles from the uncoupled to the fully coupled case. In our approach experimental resonances correspond to the S matrix poles in the complex energy plane close to the physical region. This is in contrast with some other descriptions where the resonance parameters are introduced using K matrix poles or Breit–Wigner formulae with some ad hoc background in each channel. Let us here remark that the Particle Data Group [1] has misplaced the σ meson parameters found in [9]. They have been referred to under the name "$f_0(400–1200)$ Breit–Wigner mass or K matrix pole parameters" on page 363 of [1] instead of being referred under the appropriate title "$f_0(400–1200)$ T matrix pole $\sqrt{s}$". Similar misplacements were also made on pages 392 and 393 for the $f_0(1370)$. Studying the analytical structure of the multichannel amplitudes we shall show the important role played not only by the poles but also by the zeroes of the S matrix. Knowledge of the poles and zeroes enables us to give in some cases a simple phenomenological approximation of the T matrix. Our results on the scalar–isoscalar resonances, masses, widths, branching ratios, coupling constants as well as on the phase shifts, inelasticities and cross sections in the three channels will be discussed for our different solutions and compared with the available data.

In Sect. 2 we describe the two new solutions found in addition to those previously presented in [7]. Section 3 contains an analysis of the positions of the S matrix poles in the three-channel amplitudes. Section 4 describes the influence of the S matrix poles and zeroes on the phase shifts and inelasticities near the $f_0(1400)$ resonance. In Sect. 5 we comment on the limited applicability of the Breit–Wigner approach in multichannel meson scattering. An evaluation of branching ratios in two and three coupled channels is presented in Sect. 6 and coupling constants are discussed in Sect. 7. In Sect. 8 we present phenomenological parametrizations of multichannel amplitudes. A summary and conclusions are given in Sect. 9. In Appendix A the full formula for the Jost function of our three-channel model is supplied. Approximated formulae for the pion–pion S matrix element, especially useful in the vicinity of the $f_0(1400)$ resonance, are given in Appendix B.

2 New and former solutions

In [7] we have briefly presented our three-channel model of meson–meson scattering. This model simultaneously describes nine reactions in a unitary way. In addition to the $\pi\pi$ and $K\overline{K}$ channels an effective $\sigma\sigma$ channel is introduced in order to describe important 4π production and rescattering processes. Here we use exactly the same notation and definitions as in [7]. We furthermore give, in Appendix A, the full formula for the Jost function $D(k_1, k_2, k_3)$. Knowledge of it is sufficient to construct all the S matrix elements and all the physical quantities which will be discussed in this paper. In [7] we have obtained four three-channel solutions called A, B, C and D based on χ^2 fits to the $\pi\pi$ S wave isoscalar phase shifts and inelasticities, and to the $K\overline{K}$ phase shifts. The parameters of the separable potentials, for all the different solutions, have been obtained by fitting the results of the fully coupled channel calculations to the experimental data. If the interchannel couplings are switched off then the $K\overline{K}$ pair remains unbound in all four fits. In solutions B, C and D the $K\overline{K}$ potential is repulsive, so a $K\overline{K}$ bound state cannot be formed. In fit A the $K\overline{K}$ potential is attractive but its strength is too small to form a bound state. The parameters of the $K\overline{K}$ interactions found in [7] were different from the $K\overline{K}$ parameters obtained in [9] where a $K\overline{K}$ bound system could be formed in the absence of the interchannel interactions. We should, however, remember that in [9] a different $\pi\pi$ phase-shift solution, obtained from the data analysis on an unpolarized target by the CERN–Munich group [16], was used.

In [7] we have used several sets of the $\pi\pi$ phase shifts obtained in [8] from the data taken on a polarized target by the CERN–Cracow–Munich collaboration [17]. Now, one can ask if the data of [8] rule out any set of potential parameters leading to a $K\overline{K}$ bound state. Therefore, we have repeated the χ^2 fits performed in [7] for the "down-flat" $\pi\pi$ solution by adding an additional constraint, namely that the $K\overline{K}$ potential is sufficiently strong to obtain a bound state in the uncoupled case. As a result of these studies we have obtained two new solutions E and F which will be described below. Similar studies could be done for the "up-flat" solutions C and D which have poorer χ^2 values as seen in Table 2 of [7].

The resulting potential parameters for the solutions E and F are presented in Table 1. For solution E we can notice a particularly strong repulsive coupling constant Λ_{33} in the $\sigma\sigma$ channel. So the $\sigma\sigma$ interaction for solution E will not form any bound state when the interchannel couplings are set equal to zero. This is in contrast with solution B, where such a state exists. The $\sigma\sigma$ bound state is also present in solution F which has in addition a bound $K\overline{K}$ state. In Table 2 we give the binding properties when couplings between channels are switched off and the different χ^2 values of the four solutions A, B, E and F. The χ^2 values for solution F are not as good as for the solutions A and B, but they are still quite reasonable. The $\pi\pi$ phase shifts of solution F increase by almost 180° at $E \approx 1350$ MeV since at this energy a very narrow res-

Table 1. Separable potential parameters for the solutions E and F. Values of β and m_3 are given in GeV

Parameter	Solution E	Solution F
$\Lambda_{11,1}$	$-.26349 \times 10^{-3}$	$-.13678 \times 10^{-3}$
$\Lambda_{11,2}$	$-.18316$	$-.17845$
Λ_{22}	$-.60400$	$-.52087$
Λ_{33}	$.17703 \times 10^{2}$	$-.73962$
$\Lambda_{12,1}$	$.28776 \times 10^{-4}$	$.89713 \times 10^{-6}$
$\Lambda_{12,2}$	.036838	.048444
$\Lambda_{13,1}$	$-.34811 \times 10^{-3}$	$-.14046 \times 10^{-3}$
$\Lambda_{13,2}$	.55929	.095244
Λ_{23}	-1.5951	$-.024116$
$\beta_{1,1}$	$.16355 \times 10^{4}$	$.31518 \times 10^{4}$
$\beta_{1,2}$	1.1052	1.0712
β_2	1.4960	2.1224
β_3	.092701	1.4958
m_3	.675	.680

Table 2. Comparison of four solutions fitted to the "down-flat" data of [8]. The second and third rows indicate the presence or absence of bound states in the $K\overline{K}$ and $\sigma\sigma$ channels when interchannel couplings are switched off. In the remaining rows the different χ^2 values are specified. Numbers of experimental points are indicated in parentheses. The $\overline{\chi^2}$ values result from fitting with reduced η errors as explained in [7]

Solution	A	B	E	F
bound $K\overline{K}$	no	no	yes	yes
bound $\sigma\sigma$	no	yes	no	yes
χ^2_π (65)	63.0	61.2	64.8	65.4
$\chi^2_{\pi K}$ (21)	15.9	9.7	17.7	24.7
χ^2_η (30)	13.2	12.9	12.6	10.5
$\chi^2_{\rm tot}$ (116)	92.1	83.8	95.1	100.6
$\overline{\chi^2_\eta}$ (30)	36.7	29.3	33.4	33.6
$\overline{\chi^2_{\rm tot}}$ (116)	115.6	100.1	115.9	123.7

onance ($\Gamma \approx 0.5\,$MeV) is created about 10 MeV below the $\sigma\sigma$ threshold. This resonance also makes very narrow structures in the energy dependence of the $\pi\pi$ inelasticity and phase shifts. However, they cannot be uniquely confirmed by the existing data, so we tend to treat solution F as an interesting but experimentally not well confirmed example of a phenomenological set of separable potential parameters. The χ^2 numbers of solution E are better than those of solution F. They are comparable to those of solution A; however, solution B has the best χ^2. Therefore, in the following mainly the three solutions A, B and E will be simultaneously discussed. We shall furthermore present new physical quantities like cross sections, branching ratios and coupling constants which have not been discussed in [7].

In Fig. 1 we compare, for energies above 1350 MeV ($\sigma\sigma$ threshold), the inelasticities for solution E in the three channels. Both the $\pi\pi$ and the $K\overline{K}$ inelasticities show a minimum with different depths near 1600 MeV and 1650 MeV, respectively. The $\sigma\sigma$ inelasticity, however, has two minima at 1475 and 1675 MeV. The second minimum can be related to an additional scalar resonance at about 1700 MeV ($f_0(1710)$). The appearance of this resonance in addition to $f_0(1400)$ is a unique feature of solution E. No such state exists in solutions A and B as will be shown in detail in the next chapter. As we can see in Fig. 2, this state does not produce any strong increase of the $\pi\pi$ phase shifts which is often expected in the vicinity of a resonance. This fact will be explained in the next section.

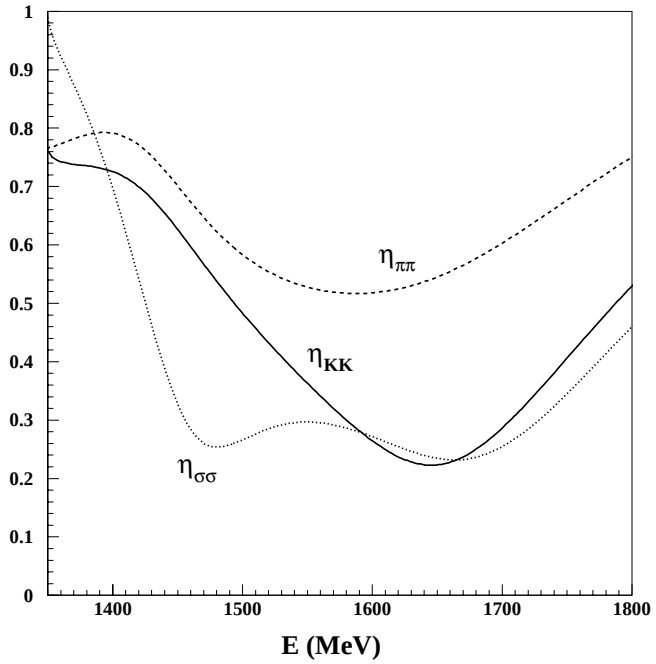

Fig. 1. Energy dependence of inelasticity in the $\pi\pi$, $K\overline{K}$ and $\sigma\sigma$ channels for solution E

In Fig. 3a,b we show inelasticities and phase shifts in the $\sigma\sigma$ channel for the three solutions A, B and E. Lack of resonances above 1600 MeV for the solutions A and B is responsible for a smooth energy dependence of the corresponding $\sigma\sigma$ inelasticities above 1500 MeV. A smooth decrease is also visible in the $\sigma\sigma$ phase shifts above 1450 MeV. The influence of the $f_0(1400)$ resonance on the $\sigma\sigma$ phase shifts can be seen for the solutions A and B as a small maximum around 1450 and 1400 MeV, respectively. In solution E a monotonical decrease is disturbed by two structures around 1425 and 1625 MeV, related to the $f_0(1400)$ and $f_0(1710)$ states, respectively. The "β" curve in Fig. 3b will be discussed in the next section.

3 Positions of poles

Knowledge of the positions of the S matrix poles in the complex energy plane is important for a physical interpretation of the resonances. Some information about the

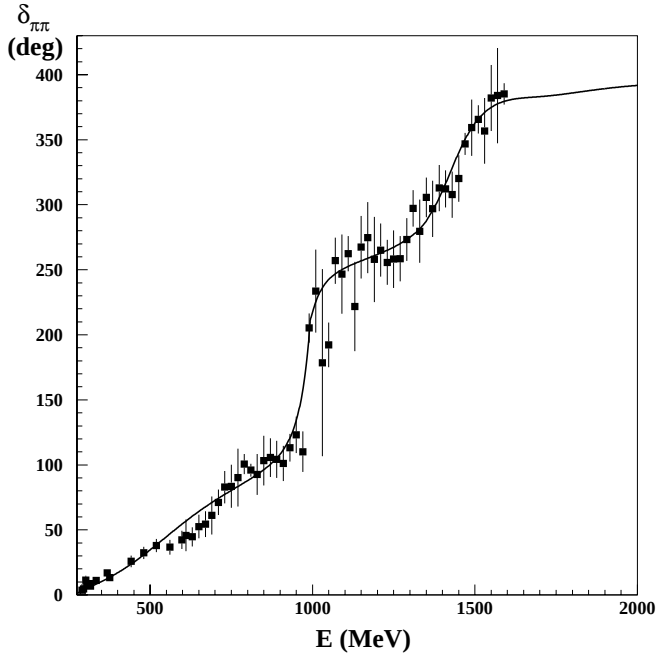

Fig. 2. Energy dependence of $\pi\pi$ phase shifts for solution E

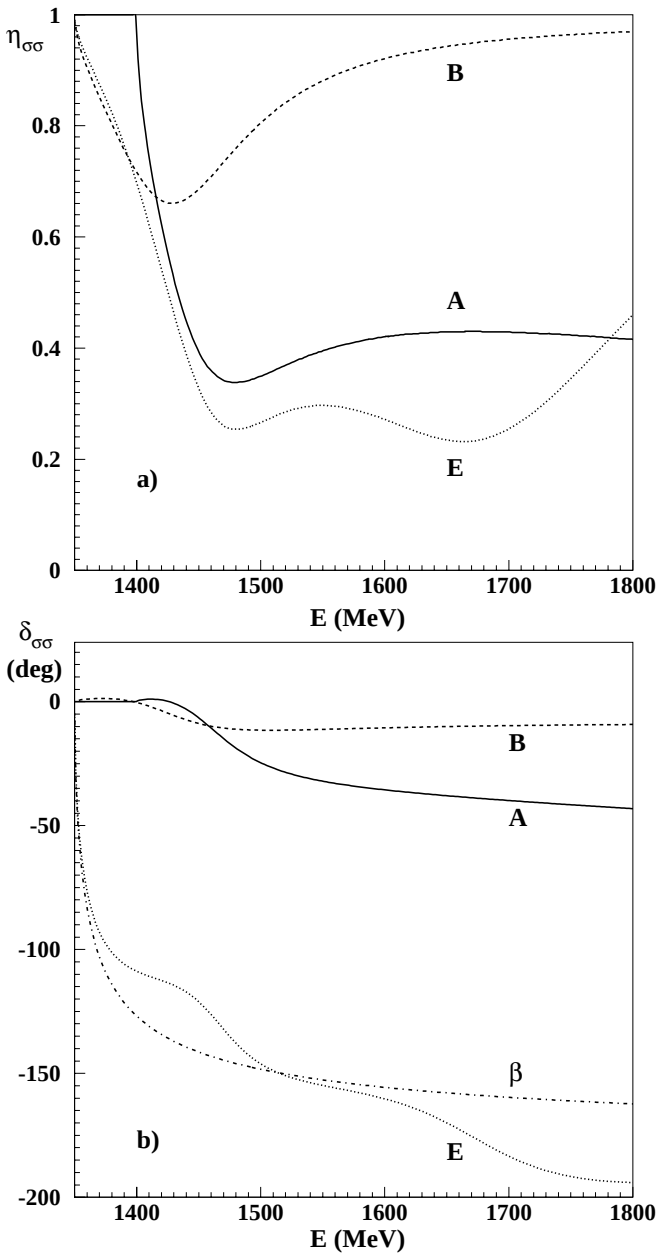

Fig. 3. Energy dependence for the solutions A, B and E of $\sigma\sigma$ inelasticities **a** and $\sigma\sigma$ phase shifts **b**. The curve denoted by β is the contribution of the double pole at $k_3 = -\mathrm{i}\beta_3$ for solution E

positions of the poles was already given in [7] for four solutions: A and B corresponding to the "down-flat" data of [8] and C and D corresponding to the "up-flat" data. Now we shall discuss in more detail three sets of poles, all corresponding to the "down-flat" data, namely the solutions A, B and E which were described in the previous section. We think that the general structure of the solutions C and D is similar to those of sets A or B. In all solutions S matrix poles appear on different sheets of the complex channel momenta k_1, k_2, k_3. The sheets can be classified according to the signs of $\mathrm{Im}\, k_1, \mathrm{Im}\, k_2, \mathrm{Im}\, k_3$. For instance, the notation $--+$ means that $\mathrm{Im}\, k_1 < 0$, $\mathrm{Im}\, k_2 < 0$ and $\mathrm{Im}\, k_3 > 0$. The positions of the most important poles for the resonances $f_0(500)$, $f_0(980)$ and $f_0(1400)$ were given in Table 3 of [7]. The origin of the resonances can be studied by a gradual decrease of the interchannel coupling constants. In this way, starting from the case where all interchannel couplings are present, we arrive at the uncoupled case and obtain a trajectory linking the positions of a given pole from the fully coupled to the corresponding fully uncoupled case. The structure of the poles for the various solutions is significantly different. Details of the positions of different S matrix poles without and with couplings between channels are given in Tables 3 to 6 for solutions A, B, E and F, respectively. In the last two columns the pole-sheet specification and their labels are given.

Let us recall that a given pole in the uncoupled channel splits into four poles in the coupled-channel case since coupling of a given channel to any other channel doubles the number of related poles. This is a consequence of the analytic structure of the Jost function $D(k_1, k_2, k_3)$ describing three coupled channels. Furthermore, one should recall that

$$D(k_1, k_2, k_3) = D^*(-k_1^*, -k_2^*, -k_3^*); \qquad (1)$$

therefore, for a given zero of $D(k_1, k_2, k_3)$ at k_1, k_2, k_3 there always exists a twin zero at $-k_1^*, -k_2^*, -k_3^*$. In the complex energy plane a pole and its twin are symmetric with respect to the imaginary energy axis. In an uncoupled-channel case zeroes and poles of the S matrix lie symmetrically with respect to the real energy axis. This symmetry

is broken when the interchannel couplings are switched on. Therefore, the asymmetry in the localization of the zeroes is crucial for understanding the energy dependence of the phase shifts and inelasticities in all the coupled channels. Now we will discuss specific features of the different solutions. The positions of the S matrix poles corresponding to the solutions A, B, E and F will be given in Tables 3, 4, 5 and 6, respectively. The "with couplings" column corresponds to the fully coupled model fitted to the data, while the "no coupling" column corresponds to the same solution with interchannel coupling switched off.

3.1 Solution A

For solution A the $\pi\pi$ channel poles at $E = (658 - \mathrm{i}607)$ MeV and $E = (1346 - \mathrm{i}275)$ MeV in the uncoupled case evolve differently when the interchannel couplings are switched on (see Table 3).

The first pole leads to a set of poles related to $f_0(500)$ at lower energy (poles I, II, and IV) while the second one splits into four states related to $f_0(1400)$ at higher energy (poles VI to IX). The pole in the $K\overline{K}$ channel at $E = (881 - \mathrm{i}498)$ MeV, lying far from the physical axis in the uncoupled case, moves to the $K\overline{K}$ quasi-bound state at $E = (988 - \mathrm{i}31)$ MeV on sheet $-++$ (pole XIV). This is the $f_0(980)$ resonance which lies quite close to the physical axis and therefore strongly influences the behavior of the $\pi\pi$ scattering phase shifts near the $K\overline{K}$ threshold. The pole trajectory linking the corresponding poles in the uncoupled and coupled cases is drawn as a solid line in Fig. 4a. In this figure we have also indicated at several intermediate positions the percentage strengths of the reduced interchannel couplings. The same broad $K\overline{K}$ pole can also move to the pole XIII at $E = (1038 - \mathrm{i}204)$ MeV on sheet $-+-$. Its trajectory is drawn as a dotted line in Fig. 4a. Poles III, V, X and XI, lying on the real axis with an energy below the $\pi\pi$ threshold, appear when the interchannel coupling strengths are large enough. Their influence on the $\pi\pi$ phase shifts is, however, small.

The extremely wide pole in the third channel at $E = (118 - \mathrm{i}2227)$ MeV goes to very distant states at energies above 3000 MeV. These states, present only in solutions A and B, are quite model dependent. They cannot be visible in the energy dependence of phase shifts or inelasticities in the three open channels. Here we only give their positions in order to illustrate the analytical structure of the model amplitudes. In many phenomenological applications such distant poles are treated as background described by additional parameters fitted separately to the data. We should stress that in our model there is no need to introduce any kind of artificial background. Large values of the interchannel coupling constants (Table 1 in [7]) are responsible for the large pole shifts as seen in Table 3 and Fig. 4a. This also applies to other solutions considered below, especially to solution B (see Tables 1, 4 to 6 and Fig. 4b).

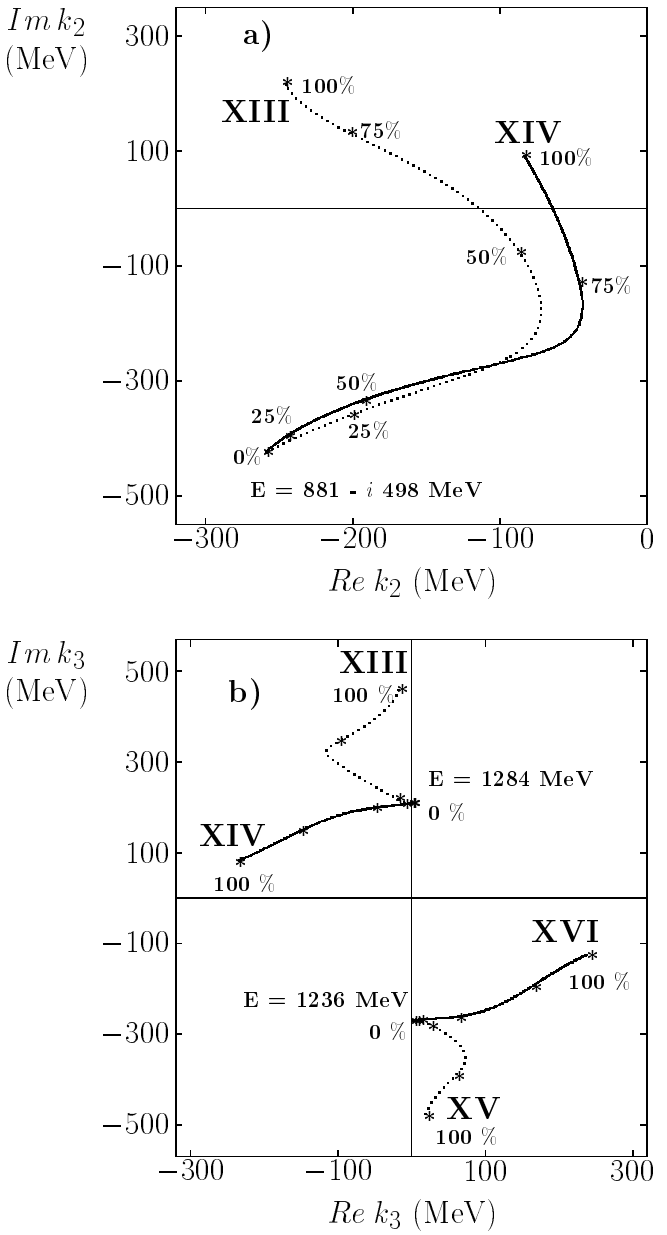

Fig. 4. Pole trajectories in the complex momentum plane as a function of the percentage of the interchannel coupling strength: **a** for solution A in the $K\overline{K}$ channel, **b** for solution B in the $\sigma\sigma$ channel. Roman numbers and energies are taken from Table 3 for **a** and from Table 4 for **b**

3.2 Solution B

For solution B (Table 4) there are two wide poles lying far from the physical axis in the uncoupled $\pi\pi$ channel.

The first pole at (733−i583) MeV splits into four states, I to IV. Pole II on sheet $-++$ and the corresponding zero lie close to the physical axis. Such a pole has an important influence on the $\pi\pi$ scattering amplitude below 1 GeV and can be related to the $f_0(500)$ resonance. The second pole evolves from $(999 - \mathrm{i}323)$ MeV into a pair of

Table 3. Positions of S matrix poles for solution A (in MeV)

Channel	No couplings		With couplings		Sign of			
	$\mathrm{Re}\,E$	$\mathrm{Im}\,E$	$\mathrm{Re}\,E$	$\mathrm{Im}\,E$	$\mathrm{Im}\,k_\pi$	$\mathrm{Im}\,k_K$	$\mathrm{Im}\,k_\sigma$	No.
			564	−279	−	−	−	I
			518	−261	−	+	+	II
$\pi\pi$	658	−607	211	0	−	+	−	III
			532	−315	−	−	+	IV
			235	0	+	+	−	V
			1405	−74	−	−	−	VI
$\pi\pi$	1346	−275	1445	−116	−	+	+	VII
			1424	−94	−	+	−	VIII
			1456	−47	−	−	+	IX
			170	0	+	−	−	X
			159	0	−	−	−	XI
$K\overline{K}$	881	−498	418	−10	−	−	+	XII
			1038	−204	−	+	−	XIII
			988	−31	−	+	+	XIV
			4741	−4688	−	−	−	XV
$\sigma\sigma$	118	−2227	3687	−2875	−	+	−	XVI
			3626	−3456	+	−	−	XVII
			3533	−579	+	+	−	XVIII

Table 4. Positions of S matrix poles for solution B (in MeV)

Channel	No couplings		With couplings		Sign of			
	$\mathrm{Re}\,E$	$\mathrm{Im}\,E$	$\mathrm{Re}\,E$	$\mathrm{Im}\,E$	$\mathrm{Im}\,k_\pi$	$\mathrm{Im}\,k_K$	$\mathrm{Im}\,k_\sigma$	No.
			332	−114	−	−	−	I
$\pi\pi$	733	−583	511	−266	−	+	+	II
			512	−266	−	+	−	III
			332	−115	−	−	+	IV
			900	−13	−	−	−	V
$\pi\pi$	999	−323	1441	−125	−	+	+	VI
			1430	−149	−	+	−	VII
			942	−25	−	−	+	VIII
			3670	−2263	−	−	−	IX
$K\overline{K}$	2744	−1698	3664	−2240	−	−	+	X
			3102	−940	+	−	−	XI
			3104	−904	+	−	+	XII
			992	−34	−	+	+	XIII
$\sigma\sigma$	1284	0	1421	−54	−	−	+	XIV
			956	−36	−	+	−	XV
$\sigma\sigma$	1236	0	1411	−85	−	−	−	XVI

poles at $(1441 - \mathrm{i}125)$ and $(1430 - \mathrm{i}149)\,\mathrm{MeV}$, both related to the $f_0(1400)$ resonance. The two other shifted poles V and VIII remain close to 900 MeV. A very broad pole at $(2744 - \mathrm{i}1698)\,\mathrm{MeV}$ in the uncoupled $K\overline{K}$ channel leads to four poles IX to XII lying far away from the physical region. Their influence on the scattering amplitudes is negligible. In Fig. 4b four interesting trajectories in the k_3 complex plane are drawn. The $\sigma\sigma$ bound state at 1284 MeV ($\mathrm{Im}\,k_3 > 0$) can either evolve to the $f_0(980)$ resonance (pole XIII) at $(992 - \mathrm{i}34)\,\mathrm{MeV}$ (dotted line) or to the $f_0(1400)$ (pole XIV) at $(1421 - \mathrm{i}54)\,\mathrm{MeV}$ (solid line). Similarly the so-called quasi-bound state at 1236 MeV ($\mathrm{Im}\,k_3 < 0$) can either go to the pole XV at $(956 - \mathrm{i}36)\,\mathrm{MeV}$ closely related to the $f_0(980)$ (dotted line) or to the $f_0(1400)$ resonance (pole XVI) at $(1411 - \mathrm{i}85)\,\mathrm{MeV}$ (solid line).

Table 5. Positions of S matrix poles for solution E (in MeV)

Channel	No couplings		With couplings		Sign of			
	Re E	Im E	Re E	Im E	Im k_π	Im k_K	Im k_σ	No.
			600	−355	−	−	−	I
$\pi\pi$	542	−307	533	−254	−	+	+	II
			533	−246	−	+	−	III
			600	−354	−	−	+	IV
			1421	−79	−	−	−	V
$\pi\pi$	1473	−150	1441	−106	−	+	+	VI
			1428	−104	−	+	−	VII
			1466	−38	−	−	+	VIII
			328	−7	−	−	−	IX
$K\overline{K}$	441	0	336	−8	−	−	+	X
			978	−46	−	+	−	XI
$K\overline{K}$	990	0	990	−34	−	+	+	XII
			1703	−271	−	−	−	XIII
$\sigma\sigma$	1565	−112	1648	−67	−	+	−	XIV
			1673	−77	−	−	+	XV
			1624	−175	+	−	−	XVI

3.3 Solution E

In Table 5 the positions of the poles for solution E are shown. The first pole at $(542 - \mathrm{i}307)$ MeV evolves (as for solution B) to four wide states. One of these (pole II) at $(533 - \mathrm{i}254)$ MeV on sheet $-++$ lies close to the physical region and can be related to $f_0(500)$. When the interchannel couplings are switched on, the second pole at $E = (1473 - \mathrm{i}150)$ MeV, coming from the $\pi\pi$ channel in the uncoupled-channel case, creates the four poles V to VIII. Pole V on sheet $---$ and a zero related to pole VI on sheet $-++$ are responsible for an increase of the $\pi\pi$ phase shifts around 1400 MeV (see Fig. 2). Looking at the inelasticities η_π and η_K in Fig. 1 one can see small bumps around 1400 MeV caused by pole V.

The $K\overline{K}$ antibound state at 441 MeV transforms into two states IX and X lying far away from the physical axes in the $K\overline{K}$ and $\sigma\sigma$ complex momentum spaces. The $K\overline{K}$ bound state in the uncoupled case lies very close to the $K\overline{K}$ threshold at $E = 990$ MeV and can evolve, when interchannel couplings are switched on, into two narrow states (poles XI and XII) on sheets $-+-$ and $-++$. Pole XII on sheet $-++$ lies closer to the physical region than pole XI and can therefore be related to $f_0(980)$. The last resonance at $(1565 - \mathrm{i}112)$ MeV evolves into four states at about 1700 MeV. As can be seen in Fig. 2, the $\pi\pi$ phase shifts do not strongly increase around 1700 MeV. This fact is related to the positions of two singularities of the S matrix having the strongest influence on the $\pi\pi$ scattering amplitude. One of them is pole XIII on sheet $---$ and the second is a zero also lying on sheet $---$ related to pole XVI on sheet $+--$. The zero and the pole lie on the same sheet, so they partially cancel each other and their influence on the energy dependence of the $\pi\pi$ amplitude is unusually small. The zero lies closer to both real and imaginary energy axes than the pole. Therefore, in Fig. 2 a flat energy dependence of the $\pi\pi$ phase shifts between 1600 and 1750 MeV is seen as well as a smooth increase above 1750 MeV where the influence of the pole becomes larger than the action of the zero.

Another particular case of the influence of the S matrix singularities on the scattering amplitudes can be seen in Fig. 3b. A strong decrease of the $\sigma\sigma$ phase shifts for solution E, very well visible near the threshold at 1350 MeV, can be understood if we take into account all the singularities of the S_{33} element of the S matrix. For this solution the value of parameter β_3 is very small ($\beta_3 = 92.7$ MeV) so the double zero of S_{33} at $k_3 = -\mathrm{i}\beta_3$ is the closest singularity to the $\sigma\sigma$ threshold. This zero of S_{33} is a result of the Jost function double pole at $k_3 = -\mathrm{i}\beta_3$ as can be seen in the analytical expression for J_{33} given in (A9) of [9]. One can calculate the $\sigma\sigma$ phase shifts keeping only this pole contribution to J_{33}. The result is drawn in Fig. 3b as the dotted line denoted by "β". Comparison with the full calculation shows the dominance of this singularity over a large energy range. The poles related to the $f_0(1400)$ and $f_0(1710)$ only slightly disturb the energy dependence of the $\sigma\sigma$ phase shifts at about 1425 and 1625 MeV. This example shows that one cannot extract complete information about the resonances from the energy dependence of the phase shifts. One also needs to know the analytical structure of the S matrix singularities. Let us note here that in the Particle Data Table [1] there is a state called $f_J(1710)$ in a mass range similar to that of our $f_0(1710)$, with the $J = 0$ possibility not excluded. It has been recently shown that this $J = 0$ assignment is more favorable than the $J = 2$ one [18].

3.4 Solution F

In solution F there are both $K\overline{K}$ and $\sigma\sigma$ bound states in the uncoupled-channel case (see Tables 2 and 6). In the fully coupled case, the $\sigma\sigma$ quasi-bound state with a width of about 0.5 MeV generates a very narrow 180° jump of the $\pi\pi$ phase shifts at about 1350 MeV. The appearance of such a not well confirmed resonance cannot be excluded since the precision of the existing data is rather limited and the χ^2 values for solution F are still acceptable. Apart from this narrow state, solution F is similar to other solutions so in the further analysis we shall not study the properties of this solution in detail.

By comparing different solutions we have seen that similar relatively narrow resonances can emerge from very different poles in the uncoupled-channel cases depending on the set of the interaction parameters. Therefore, one would need more data of a better precision to disentangle the phenomenologically good solutions A, B and E. In the next section we shall further discuss other properties of the meson–meson scattering amplitudes.

4 Influence of S matrix poles and zeroes on phase shifts and inelasticities near the $f_0(1400)$ resonance

The properties of the scattering and production amplitudes in the energy region near 1400 MeV can be understood provided that we know the positions of the S matrix singularities, especially the poles and zeroes close to the physical region. In the previous chapter we have seen that the S matrix has many poles lying on different sheets. Now we would like to choose the most important poles and zeroes which influence the phase shifts and inelasticities and determine the resonance parameters. The S matrix elements S_{ij} $(i,j=1,2,3)$ can be written in terms of the Jost function of different arguments, for example

$$S_{11}=\frac{D(-k_1,k_2,k_3)}{D(k_1,k_2,k_3)}. \tag{2}$$

Expressions for some other matrix elements can be found in [19]. All S matrix elements are inversely proportional to the Jost function $D(k_1,k_2,k_3)$ which has a zero on sheet $---$ at the channel momenta k_{id} $(i=1,2,3)$:

$$D(k_{1d},k_{2d},k_{3d})=0. \tag{3}$$

The corresponding energy E_d in the complex plane is given by

$$E_d=2\sqrt{{k_{1d}}^2+{m_1}^2}=2\sqrt{{k_{2d}}^2+{m_2}^2}=2\sqrt{{k_{3d}}^2+{m_3}^2}, \tag{4}$$

where m_i denote the meson masses. The energies E_d on sheet $---$ corresponding to the $f_0(1400)$ resonance are collected in Table 7 for our solutions A, B, E and F. Knowledge of this pole position of the S matrix is, however, not sufficient to describe the pion–pion phase shifts and inelasticities even at the energy closest to the pole. We should also know the *zero* of the numerator $D(-k_1,k_2,k_3)$ on sheet $+++$ close to the physical axis. This zero is in turn related to the zero of the denominator $D(k_1,k_2,k_3)$ on sheet $-++$. The corresponding energies on sheet $-++$ are also given in Table 7. We can notice that both the real and the imaginary parts of the energy are shifted on sheet $-++$ if we compare them with the corresponding parts of the energy on sheet $---$. The values of the phase shifts and the inelasticities depend on the zero of the numerator $D(-k_1,k_2,k_3)$ and on the zero of the denominator $D(k_1,k_2,k_3)$. This means that by measurements of the $\pi\pi$ phase shifts and inelasticities we cannot uniquely determine one single value of the resonance energy and one value of the resonance width related to the imaginary part of the energy. Strong interchannel couplings are responsible for the energy shifts of the zeroes found on different sheets.

In the vicinity of the $f_0(1400)$ resonance one can, however, build up an approximation to the S matrix elements in three channels. This will furthermore allow us to understand the role played by the four poles whose energy positions in the different sheets are given in Table 7 for our four solutions A, B, E and F. We make an expansion of the Jost function $D(k_1,k_2,k_3)$ near its zero on sheet $---$ at (k_{1d},k_{2d},k_{3d}):

$$D(k_1,k_2,k_3)\approx(k_1-k_{1d})d_1. \tag{5}$$

Let us denote by k_{in} $(i=1,2,3)$ the zero position of the same Jost function on sheet $-++$. Then in a first approximation

$$D(-k_1,k_2,k_3)\approx(k_1-k_{1n}^*)c_1. \tag{6}$$

Here d_1 and c_1 are complex constants. The quantity $1/d_1$ is the residue of the $1/D(k_1,k_2,k_3)$ pole on sheet $---$ and $1/c_1$ is the residue of the pole on sheet $-++$. Here we have used the property of the Jost function expressed by (1). The twin zero may sometimes be closer than the pole on sheet $---$ to the physical region and therefore it can strongly influence the S matrix element. The $\pi\pi$ S matrix element can then be approximated by

$$S_{11}=\frac{k_1+p_1}{k_1-k_{1d}}f_1, \tag{7}$$

where $f_1=c_1/d_1$ and $p_1=-k_{1n}^*$. Similarly the $K\overline{K}$ and $\sigma\sigma$ S matrix elements can be written as

$$S_{22}=\frac{D(k_1,-k_2,k_3)}{D(k_1,k_2,k_3)}\approx\frac{k_2+p_2}{k_2-k_{2d}}f_2, \tag{8}$$

$$S_{33}=\frac{D(k_1,k_2,-k_3)}{D(k_1,k_2,k_3)}\approx\frac{k_3+p_3}{k_3-k_{3d}}f_3, \tag{9}$$

where f_2 and f_3 are complex constants, p_2 is the kaon complex momentum on sheet $-+-$ and p_3 is the σ momentum on sheet $--+$ for which the Jost functions in the numerators vanish.

We have numerically checked, by comparison with the exact values, that the phase shifts and inelasticities for the

Table 6. Positions of S matrix poles for solution F (in MeV)

Channel	No couplings		With couplings		Sign of			
	Re E	Im E	Re E	Im E	Im k_π	Im k_K	Im k_σ	No.
			691	−511	−	−	−	I
$\pi\pi$	554	−377	528	−255	−	+	+	II
			673	−410	−	+	−	III
			658	−379	−	−	+	IV
			1387	−81	−	−	−	V
$\pi\pi$	1407	−80	1428	−93	−	+	+	VI
			1367	−79	−	+	−	VII
			1447	−77	−	−	+	VIII
			486	−5	−	−	−	IX
$K\overline{K}$	497	0	396	−25	−	−	+	X
			967	−31	−	+	−	XI
$K\overline{K}$	968	0	993	−42	−	+	+	XII
			250	0	−	−	−	XIII
$\sigma\sigma$	341	0	270	0	−	+	−	XIV
			1349	−0.2	−	−	+	XV
$\sigma\sigma$	1353	0	1349	−0.3	−	+	+	XVI

Table 7. Energy positions of S matrix poles related to $f_0(1400)$

Solution	Energy (in MeV)			
	sheet	sheet	sheet	sheet
	− − −	− + +	− + −	− − +
A	1405 − i74	1445 − i116	1424 − i94	1456 − i47
B	1411 − i85	1441 − i125	1430 − i149	1421 − i54
E	1421 − i79	1441 − i106	1428 − i104	1466 − i38
F	1387 − i81	1428 − i93	1367 − i79	1447 − i77

solutions A, B and E, in the region of the $f_0(1400)$ resonance (effective mass range between 1350 and 1500 MeV), are qualitatively well described by (7) to (9). For solution B the agreement is even quantitative since the percentage error is only of the order of 10% or less. This error is obtained if the coupling constants f_i are calculated using the first-order derivatives of the Jost function. The errors can be reduced further if we modify the complex factors f_1, f_2 and f_3 taking into account the second derivatives of the Jost function as explained in Appendix B. Solution E is somewhat peculiar since the region of $f_0(1400)$ is also influenced by a wide resonance, $f_0(1710)$ (see Table 5). The phase shifts in the $\sigma\sigma$ channel are additionally affected by the second-order zeroes at $k_3 = \pm i\beta_3$ since the parameter β_3 is small in that case, as already discussed in Sect. 3.3.

5 Limited applicability of the Breit–Wigner approach

We should note here that the zeroes of the Jost function $D(k_1, k_2, k_3)$ on sheets $- - -$, $- + +$, $- + -$ and $- - +$ are in general different, so the following inequalities between the corresponding complex momenta hold: $p_1 \neq k_{1d}$, $p_2 \neq k_{2d}$ and $p_3 \neq k_{3d}$. In particular, looking at Table 7 we can notice that the poles on sheet $- - +$ are shifted towards higher energy in comparison with the poles on sheet $- - -$. Also the corresponding width related to the imaginary part of the energy is considerably reduced on sheet $- - +$ for the solutions A, B and E. This fact has important consequences for the energy dependence of the phase shifts and inelasticity parameters, which will be different from those obtained using the Breit–Wigner form. Let us now compare the approximations to the diagonal S matrix elements (7) to (9) and the Breit–Wigner multichannel formula for the transition matrix elements

$$T_{ij}^{\mathrm{BW}} = \frac{1}{\sqrt{k_i k_j}} \frac{M\Gamma}{M^2 - s - \mathrm{i}M\Gamma} c_i c_j. \tag{10}$$

In this equation, M is the mass and Γ the width of a resonance, c_i, c_j are real channel branching ratios and $c_i^2 = \Gamma_i/\Gamma$, where Γ_i are the partial decay widths. These formulae are valid if the resonance pole dominates the transition amplitude in the physical region and if the background can be neglected. The corresponding diagonal elements of the S matrix expressed by

$$S_{ii}^{\mathrm{BW}} = 1 + 2\mathrm{i}k_i T_{ii}^{\mathrm{BW}} \tag{11}$$

are then written as

$$S_{ii}^{\mathrm{BW}} = \frac{s - [M^2 + \mathrm{i}M(2\Gamma_i - \Gamma)]}{s - (M^2 - \mathrm{i}M\Gamma)}. \tag{12}$$

Recalling that $s = E^2 = 4(k_i^2 + m_i^2)$ we can approximate (12) by

$$S_{ii}^{\mathrm{BW}} \approx \frac{k_{iN}}{k_{iD}} \frac{k_i - k_{iN}}{k_i - k_{iD}}, \tag{13}$$

where

$${k_{iD}}^2 = \frac{M^2}{4} - m_i^2 - \mathrm{i}\frac{M\Gamma}{4}, \tag{14}$$

and

$${k_{iN}}^2 = \frac{M^2}{4} - m_i^2 + \mathrm{i}\frac{M}{4}(2\Gamma_i - \Gamma). \tag{15}$$

While formally (13) looks very similar to (7), (8) and (9), it is very different from them since k_{iD} and k_{iN} have to satisfy the inequalities: $\mathrm{Re}\, k_{iN} \leq \mathrm{Re}\, k_{iD}$, $\mid \mathrm{Im}\, k_{iN} \mid \leq \mid \mathrm{Im} k_{iD} \mid$. These inequalities follow from an obvious inequality that each partial width Γ_i is smaller than the total width Γ. In fact, each Breit–Wigner S_{ii} matrix element depends only on three *real* parameters M, Γ and Γ_i while the matrix elements (7), (8) and (9) depend on three *complex* parameters: one giving the position of the zero in the denominator, the second giving the zero of the numerator and the third parameter being f_i.

The Breit–Wigner formula (10) is very often used to analyze experimental data in order to obtain a mass and a width of different resonant states [1]. It is widely believed that it should provide the *same* resonance parameters independently on the reaction channel in which the resonant signal is detected. Our analysis, however, puts some limits on the practical applicability of the Breit–Wigner approach. The point is that in each reaction channel not only the S matrix pole plays a significant role but also the accompanying zero. The pole is common to all reaction channels, but the zero is different in each channel and cannot be located simply by giving one number corresponding to a branching ratio or a channel coupling constant. This point will be discussed in detail in the two next sections. Here we can make the following remark. If one applies the Breit–Wigner formula to the data analysis in a particular channel then one obtains distorted resonance parameters which are to some extent "averaged" over the pole and accompanying zero parameters. This effect might explain the fact that some resonant parameters "measured" in one coupled channel can be different from those obtained in another channel if the phenomenological model applied in the data analyses is essentially restricted to the Breit–Wigner formula.

6 Branching ratios

Branching ratios are important parameters of hadronic resonances. Usually they are obtained from experimental data by applying the multichannel Breit–Wigner formula (10) with some background parametrization in a limited range of effective masses. In our model we do not use any arbitrary background parametrization nor the Breit–Wigner parametrization. We fully exploit our knowledge of the analytical structure of the S matrix. Some S matrix poles close to the physical range can be related to the scalar-meson resonances as already discussed in Sects. 2 and 3. From the position of a given pole in the complex energy plane we can deduce the mass of the resonance and its total width. A determination of the partial decay width in the presence of two and three open channels is, however, a more complicated issue which we are going to discuss in this section.

6.1 Definitions

Let us recall that our model satisfies the unitarity condition for the S matrix: $S^+S = 1$, and that the diagonal matrix elements are parametrized as

$$S_{jj} = \eta_j \mathrm{e}^{2\mathrm{i}\delta j}, \quad j = 1, 2, 3, \tag{16}$$

where η_j are the inelasticities and δ_j the channel phase shifts. The non-diagonal elements are related to the non-diagonal reaction T matrix elements by

$$T_{jl} = \frac{1}{2\mathrm{i}} \frac{1}{\sqrt{k_j k_l}} S_{jl}, \quad j, l = 1, 2, 3, \quad j \neq l. \tag{17}$$

Expressions for S_{jl} can be found in [19]. The diagonal T matrix elements read

$$T_{jj} = \frac{1}{2\mathrm{i}k_j} \left(S_{jj} - 1\right), \quad j = 1, 2, 3. \tag{18}$$

T matrix elements satisfy the unitarity equations. For example, in the first channel above the $\sigma\sigma$ threshold

$$\mathrm{Im}\, T_{11} = k_1 |T_{11}|^2 + k_2 |T_{12}|^2 + k_3 |T_{13}|^2. \tag{19}$$

The total cross section in the first channels reads

$$\sigma_{11}^{\mathrm{tot}} = \frac{8\pi}{k_1} \mathrm{Im}\, T_{11}. \tag{20}$$

The elastic cross section is given by

$$\sigma_{11}^{\mathrm{el}} = 8\pi |T_{11}|^2 \tag{21}$$

and the transition cross sections from channel 1 to channel $j = 2$ or 3 are expressed by

$$\sigma_{1j} = \frac{8\pi}{k_1} k_j |T_{1j}|^2. \tag{22}$$

These cross sections satisfy the equation

$$\sigma_{11}^{\mathrm{tot}} = \sigma_{11}^{\mathrm{el}} + \sigma_{12} + \sigma_{13}. \tag{23}$$

In Fig. 5 all $\pi\pi$ cross sections corresponding to solution B are shown. At low energies we see a huge peak with a maximum near 600 MeV. This can be attributed to a very wide scalar σ meson. Near 1 GeV one notices a very deep and narrow minimum which is related to the $f_0(980)$ meson.

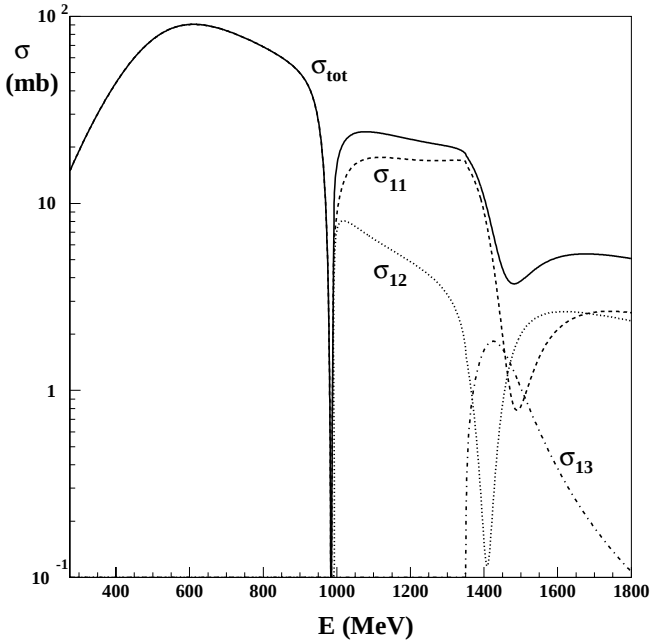

Fig. 5. Energy dependence of cross sections σ_{ij} for solution B

The fact that this resonance is seen as a dip and not, as in most cases, as a maximum of the total cross section, is due to the special value of the elastic $\pi\pi$ phase shift which goes through 180° slightly below 1 GeV. If this happens below the $K\overline{K}$ threshold the total cross section is equal to 0. The next minimum of the total cross section is near 1500 MeV, where another resonance, $f_0(1500)$, appears. Up to the $K\overline{K}$ threshold the $\pi\pi$ scattering is elastic but above the $K\overline{K}$ threshold the $\pi\pi$ to $K\overline{K}$ transition cross section becomes visible. The transition to the $\sigma\sigma$ channel is clearly visible above the third threshold at about 1350 MeV.

Numbers of meson pairs produced in each channel are proportional to the cross sections defined above so for example in the $\pi\pi$ channel we can define three branching ratios:

$$b_{1j} = \frac{\sigma_{1j}}{\sigma_{11}^{\rm tot}} \ , \quad j = 1, 2, 3. \tag{24}$$

These branching ratios obviously satisfy

$$b_{11} + b_{12} + b_{13} = 1. \tag{25}$$

Cross sections similar to σ_{1j} and the corresponding branching ratios can be defined in channels 2 and 3 by changing index 1 into 2 and 3, respectively. In this way one can obtain nine branching ratios b_{ij} $(i, j = 1, 2, 3)$. All these quantities as well as the cross sections are functions of the energy or of the effective mass. Below the third threshold where the energy is smaller than $2m_3$ but greater than $2m_2$ the branching ratio matrix b_{ij} reduces to 2×2 matrix containing only four non-zero matrix elements b_{11}, b_{12}, b_{21} and b_{22}. If the T matrix is approximated by the Breit–Wigner formula (10) then the branching ratios are given simply by

$$b_{ij}^{\rm BW} = c_j^2. \tag{26}$$

From (26) we infer that the corresponding branching ratio matrix contains identical rows.

6.2 Discussion

We shall discuss the behavior of the branching ratios for solution B, plotted in Fig. 6, in detail. The energy dependence of the branching ratios for solutions A and E is similar to that for solution B. We do not expect that the energy behavior of the branching ratios for the "up-flat" solutions (solutions C and D in [7]) will be qualitatively different from that of the "down-flat" solutions A and B.

At first let us discuss the behavior of the "elastic" branching ratio b_{11} as a function of energy in the pion–pion channel (see Fig. 6a). At the $K\overline{K}$ threshold $b_{11} = 1$, but it decreases enormously steeply with increasing energy to about 0.6 (solution A and E), 0.55 (solution B) or 0.5 (2-channel "down-flat" solution of [7]) already at an energy close to 1 GeV. This steep decrease is related to the opening of the $K\overline{K}$ channel. Next b_{11} steadily increases to a maximum close to 0.9 for the above solutions as the energy reaches about 1.4 GeV. At this energy the third threshold is open for the solutions A, B and E. For $E > 1.4$ GeV b_{11} decreases very fast to a minimum close to 0.2 for the three cases A, B and E and to 0 for the 2-channel "down-flat" solution. Then it rises again especially steeply for the latter solution and slower for the solutions A and B. This minimum is closely related to the presence of $f_0(1400)$.

The b_{12} branching ratio is equivalent to the transition probability of two pions into a pair of two kaons. Below the third threshold $(E < 2m_3)$ $b_{12} = 1 - b_{11}$, so its behavior is completely determined by b_{11}. b_{12} rises very steeply from the $K\overline{K}$ threshold attaining a maximum near 1 GeV and then decreases to a minimum value at about 1.4 GeV (see Fig. 6a). At this energy, however, the third threshold opens and the transition to the $\sigma\sigma$ channel becomes possible as stated by (25). An effect of the interplay between the three channels is that b_{12} rises above 1.4 GeV, attaining a maximum, and then decreases rather slowly with energy for $E > 1.5$ GeV.

Above the third threshold in the $\pi\pi$ and $K\overline{K}$ channels a non-zero fraction of the channel total cross section originates from the transition to the $\sigma\sigma$ state. In the $\pi\pi$ channel the branching ratio b_{13} forms a regular maximum at $E = 1.48$ GeV, 1.46 GeV and 1.48 GeV for the solutions A, B and E, respectively. The width of this peak is about 110 to 120 MeV (see Fig. 6a). The position and the width of this peak corresponds very closely to the parameters determined for the total width $f_0(1500)$ by the Crystal Barrel Collaboration in different channels [1].

In the second channel the b_{21} element describes the ratio of the $K\overline{K}$ to $\pi\pi$ transition cross section to the total $K\overline{K}$ cross section. At the $K\overline{K}$ threshold the annihilation cross section σ_{21} tends to infinity and the elastic cross section is finite, therefore the b_{21} coefficient is equal to 1.

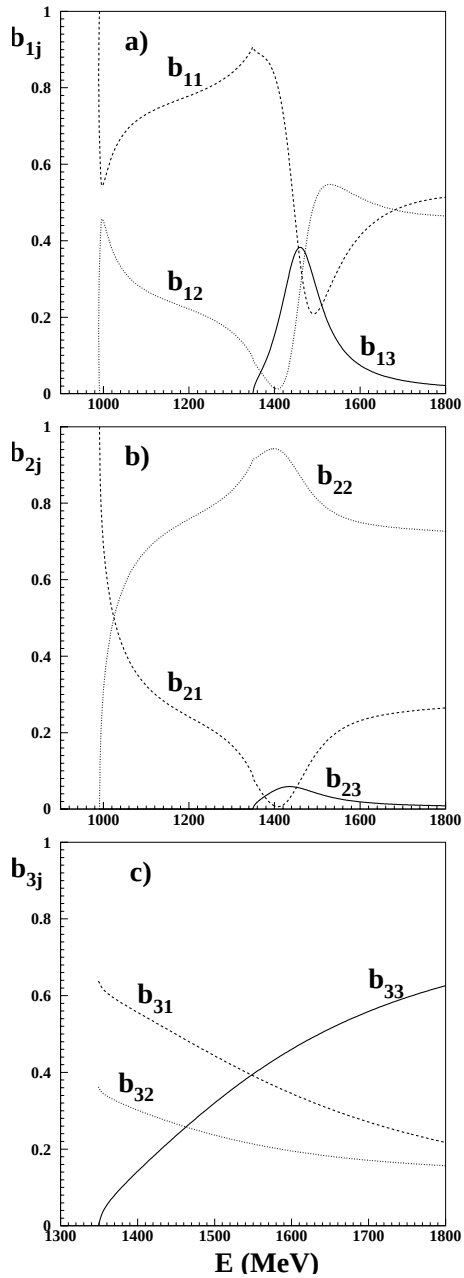

Fig. 6. Energy dependence of the branching ratios b_{ij} for solution B. The dashed line corresponds to $j = 1$, the dotted line to $j = 2$ and the solid line to $j = 3$. In **a** $i = 1$ ($\pi\pi$ channel), in **b** $i = 2$ ($K\overline{K}$ channel) and in part **c** $i = 3$ ($\sigma\sigma$ channel)

With increasing energy it decreases to a quite deep minimum close to 0 at about 1.4 GeV. At higher energy it rises slowly again for all three solutions. The transition element b_{23} starts from 0 at the $\sigma\sigma$ threshold, reaches a maximum rather quickly, and then drops smoothly (see Fig. 6b).

Two branching ratios in the third channel, namely b_{31} and b_{32}, decrease from the large values at the $\sigma\sigma$ threshold. Their behavior is characteristic for the annihilation reactions. On the contrary, the elastic branching ratio b_{33} rises monotonically with energy as shown in Fig. 6c.

Comparing Figs. 6a, b and c one can see that the Breit–Wigner formulae (26) are never satisfied above 1 GeV even in the vicinity of the well defined resonances like $f_0(980)$ and $f_0(1400)$.

6.3 Average branching ratios near the $f_0(980)$ resonance

The $f_0(980)$ resonance lies very close to the $K\overline{K}$ threshold and this fact has a very important consequence for the experimental determination of the partial widths of this resonance of the decay into the $\pi\pi$ and $K\overline{K}$ channels. The $\pi\pi$ channel is open below the $K\overline{K}$ threshold, so for this channel we can determine the averaged $\pi\pi$ branching ratio b_{11} choosing a range of the $\pi\pi$ effective mass centered at the resonance mass M_s with a maximum energy value equal to $M_{\max}$. This value should be larger than M_s by more than the resonance width. This width is still not well defined experimentally. In [1] the full width is 40 to 100 MeV. In our three-channel analyses [7] it was between 60 and 70 MeV and larger than these numbers by 10 to 30 MeV for two-channel fits. Therefore, we can choose the value $M_{\max} = 1100$ MeV as the upper limit in the integration of the $\pi\pi$ or $K\overline{K}$ effective-mass distributions. The average $\pi\pi$ branching ratio is thus defined as follows:

$$\langle b_{11}\rangle = \frac{1}{2(M_{\max} - M_s)} \int_{2M_s - M_{\max}}^{M_{\max}} b_{11}(E)\mathrm{d}E. \qquad (27)$$

The average $K\overline{K}$ branching ratio over the same energy interval is

$$\langle b_{12}\rangle = 1 - \langle b_{11}\rangle. \qquad (28)$$

Since $b_{12} = 0$ below the $K\overline{K}$ threshold

$$\langle b_{12}\rangle = \frac{1}{2(M_{\max} - M_s)} \int_{2m_2}^{M_{\max}} b_{12}(E)\,\mathrm{d}E. \qquad (29)$$

The mass values M_s corresponding to the $f_0(980)$ resonance position on sheet $-++$ are 993, 989, 992 and 990 MeV for the two-channel down-flat model and the three-channel models A, B and E, respectively [7]. After integration over the energy we have obtained averaged $\langle b_{12}\rangle$ values of 0.191, 0.156, 0.170 and 0.158 for the above four solutions corresponding to different sets of interaction parameters. The above numbers should, however, not be compared with the experimental value of $21.9 \pm 2.4\%$ quoted as $\Gamma(K\overline{K})/\left[\Gamma(\pi\pi) + \Gamma(K\overline{K})\right]$ in the previous editions of the Review of Particle Properties (see for example [20]). The reason is that the numbers written under the title "$\Gamma_{\pi\pi}/(\Gamma_{\pi\pi} + \Gamma_{KK})$" in [20,1] are the values of the inelasticity coefficient η_{av}, defined below, and therefore they are *not* equal to the partial branching ratios of $f_0(980)$. This difference is important since the branching ratios defined by (24) not only depend on the inelasticity coefficient η but also on the $\pi\pi$ and $K\overline{K}$ phase shifts.

Experimentally the $\eta_{\rm av}$ value was obtained from the data on the $\pi^- p \to K^0_{\rm S} K^0_{\rm S} n$ reaction using the relation

$$\eta^2(E) = 1 - \frac{\sigma(\pi^+\pi^- \to f_0(980) \to K^0_{\rm S} K^0_{\rm S})}{\sigma_{\rm u}}, \qquad (30)$$

where $\sigma_{\rm u} = \pi/(6k^2)$ is the unitary limit of the $\pi^+\pi^- \to K^0_{\rm S} K^0_{\rm S}$ scalar–isoscalar cross section with k being the $K^0_{\rm S}$ momentum in the $K^0_{\rm S} K^0_{\rm S}$ c.m. system. Let us remark that from the unitarity condition, below opening of the third channel, one has $\eta \equiv \eta_1 \equiv \eta_2$. Thus, one can define

$$\eta_{\rm av} = \left(\frac{1}{E_{\rm max} - 2m_K} \int_{2m_K}^{E_{\rm max}} {\rm d}E\, \eta^2(E) \right)^{1/2} \qquad (31)$$

and use $E_{\rm max} \approx 1.1\,{\rm GeV}$ as a good representation of the upper experimental limit of the $K^0_{\rm S} K^0_{\rm S}$ effective energy (see [21] for a discussion of experimental uncertainties). Experimental values of $\eta_{\rm av}$ obtained in [21–23] are equal to 0.67 ± 0.09, 0.78 ± 0.03 and $0.81^{+0.09}_{-0.04}$ respectively. Our calculations give *lower* values: 0.487, 0.496 and 0.494 for the solutions A, B and E, respectively. We have also calculated the $\eta_{\rm av}$ values 0.494 and 0.761 corresponding to the two-channel "down-flat" solution of [7] and to the two-channel set 1 result of [9], respectively. Here we should stress that the last number is a result of the fit to the data for the reactions $\pi^- p \to K^- K^+ n$ and $\pi^+ n \to K^- K^+ p$ of [15] while the four previous numbers around 0.49 are based on inelasticities measured in $\pi^- p_\uparrow \to \pi^+\pi^- n$ [8]. The difference between the above two-channel fits is therefore due to the use of different experimental data sets. Problems with the normalization of the $\pi\pi \to K\overline{K}$ cross sections have already been discussed by Morgan and Pennington in [24] (see in particular Fig. 4 therein) and Bugg, Sarantsev and Zou in [25]. The values of the inelasticity η from [8], which were later used in [7], correspond to the elastic $\pi\pi \to \pi\pi$ reaction. Although the errors are quite large, the η values found in [8] near the $f_0(980)$ resonance are visibly lower than those of [15]. This difference, however, could be partially explained by a possible contribution of channels other than $\pi\pi$ and $K\overline{K}$.

This difference between the data can also be seen in the calculation of $\langle b_{12} \rangle$. If we use the parameters corresponding to the set 1 of [9] then $\langle b_{12} \rangle = 0.055$. This low value is related to the rather low mass of $f_0(980)$, this being equal to 973 MeV, and to its width of 29 MeV as obtained in [9]. In the fits described in [7] we have obtained the $f_0(980)$ masses close to 990 MeV and substantially larger values of the $f_0(980)$ width. The authors of [9] and [26] have also improperly used another definition of "branching ratio" in their (52) and in (33) to (35), respectively. Those equations gave essentially the averaged values of $1 - \eta^2$ which should not be directly compared to $\eta_{\rm av}$.

One remark is in order here. If all transition amplitudes are dominated by a single Breit–Wigner resonance as in (10) then the branching ratio 2×2 matrix has to satisfy the following relations: $b_{21} = b_{11}$ and $b_{22} = b_{12}$. These relations are not satisfied above the $f_0(980)$ resonance energy (see Fig. 6). This means among others that the transition amplitudes cannot simply be described in terms of a single Breit–Wigner formula.

In Fig. 6a,b we see that the element b_{21} is in general larger than b_{12}, especially near the $K\overline{K}$ threshold where b_{21} tends to 1 while b_{12} goes to zero. Nevertheless, there is a rather wide range of energies between 1.15 and 1.4 GeV where both ratios are quite close each other.

6.4 Average branching ratios in the range 1100–1420 MeV

In [27] the mass range of 1100 to 1420 MeV has been chosen to compare the ratio of $\pi\pi$ to $K\overline{K}$ pairs produced by incoming pions on a polarized target at about $18\,{\rm GeV}/c$. The $K\overline{K}$ branching ratio was $6.4^{+1.6}_{-2.0}\%$.

We have calculated the average values of b_{12} in this energy region obtaining 0.189, 0.175, 0.166 and 0.167 for the two-channel "down-flat" and three-channel solutions A, B and E, respectively. These values are higher than the experimental result of [27]. One should, however, remember that the experimental errors of the phase shifts and inelasticities are large (see [7]) so the theoretical errors of b_{12} are also large. For completeness we give the value 0.099 corresponding to the data set 1 of [9]. In order to get this value and the other four values written above we used the ordinary averaging procedure

$$\bar{b}_{12} = \frac{1}{M_{\rm max} - M_{\rm min}} \int_{M_{\rm min}}^{M_{\rm max}} b_{12}(E)\, {\rm d}E \qquad (32)$$

and not the definition (29) which is applicable only near the $K\overline{K}$ threshold. Here one should once again be reminded of the confusion concerning the definitions of the branching ratios as discussed in subsection 6c, namely that the value $B_{\rm av} = 16 \pm 1\%$ calculated in [9] should not have been compared with the experimental branching ratio $6.4^{+1.6}_{-2.0}\%$.

6.5 Average branching ratios near the $f_0(1400)$ resonance

In the presence of three open channels the branching ratio matrix $\boldsymbol{b}$ has nine elements. As already discussed in 6b, the behavior of these elements in the three different channels $\pi\pi$, $K\overline{K}$ and $\sigma\sigma$ is shown in Fig. 6 for solution B. For the solutions A and E the general shape of the curves is quite similar, although the numerical values of the various branching ratios differ. In [7] we have found that the width of the scalar resonance here called $f_0(1500)$ varies between 90 and 180 MeV, depending on the solution. Now we can choose the energy interval 1350 MeV to 1500 MeV to present the averaged values of the branching ratios in the form of 3×3 matrix. The elements of the last line of this matrix are averaged over the energies larger than the third threshold energy equal to $2m_3$. For the solutions A, B and E we obtain

$$\bar{b}_{\mathrm{A}} = \begin{pmatrix} 0.636\ 0.127\ 0.237 \\ 0.061\ 0.844\ 0.095 \\ 0.300\ 0.407\ 0.293 \end{pmatrix},$$

$$\bar{b}_{\mathrm{B}} = \begin{pmatrix} 0.608\ 0.163\ 0.229 \\ 0.054\ 0.900\ 0.045 \\ 0.529\ 0.286\ 0.185 \end{pmatrix},$$

and

$$\bar{b}_{\mathrm{E}} = \begin{pmatrix} 0.604\ 0.133\ 0.263 \\ 0.063\ 0.813\ 0.124 \\ 0.120\ 0.156\ 0.724 \end{pmatrix}.$$

In the $K\overline{K}$ channel $\bar{b}_{22}$ dominates over $\bar{b}_{21}$ and $\bar{b}_{23}$. Here the probabilities of the $K\overline{K}$ to $\pi\pi$ or $\sigma\sigma$ transitions are quite small. In the $\sigma\sigma$ channel, however, for the solutions A and B there are strong transitions from $\sigma\sigma$ to $\pi\pi$ or $K\overline{K}$, which actually are comparable to the transitions from the $\pi\pi$ channel to the $\sigma\sigma$ channels.

In [28] the branching ratios for the $f_0(1500)$ decay into the five channels $\pi\pi$, $\eta\eta$, $\eta\eta'$, $K\overline{K}$ and 4π are given as 29, 5, 1, 3 and 62%, respectively. The two main disintegration channels are $\pi\pi$ and 4π. In this model the 4π channel is represented by the effective $\sigma\sigma$ channel and we also obtain large fractions for the averaged branching ratios $\bar{b}_{11}$ and $\bar{b}_{13}$. If we calculate the ratios b_{13}/b_{11} exactly at 1500 MeV, then we obtain the values 2.4, 1.2 and 2.3 for the solutions A, B and E, respectively. These values illustrate the importance of the 4π channel, in agreement with the experimental result of [28]. In [29] the ratio $r = (B[f_0 \to K\overline{K}]/B[f_0 \to \pi\pi])\, k_1/k_2 = 0.24 \pm 0.09$ is calculated (here by f_0 we mean $f_0(1500)$). If we define the ratio $\bar{b}_{12}/\bar{b}_{11}$, then we obtain the values 0.20, 0.27 and 0.22 for the solutions A, B and E, respectively. These values are close to r. From the partial decay widths of the $f_0(1500)$ given in [25] one can calculate $\Gamma_{K\overline{K}}/\Gamma_{\pi\pi} \approx 0.10 \pm 0.05$ which is smaller than r but still consistent within the experimental errors. We know, however, that extraction of the branching ratios from experiment is a difficult task as is, for example, discussed in [30]. We should mention, however, that the average branching ratios depend quite sensitively on the energy bin chosen in the actual calculation as can be seen in Fig. 6a. Furthermore, we see that the branching ratio b_{12}, corresponding to the $\pi\pi \to K\overline{K}$ transition, is very small around 1420 MeV, close to the position of our $f_0(1400)$ resonance poles. This is in qualitative agreement with the small value for the $K\overline{K}$ branching ratio (3%) given in [28].

7 Coupling constants

Coupling constants are useful physical quantities related to the residue of the S matrix at its complex pole value

$$s_{\mathrm{R}} = M^2 - \mathrm{i}M\Gamma, \tag{33}$$

Table 8. Coupling constants of $f_0(980)$ at the pole $-++$ (in GeV^2)

Solution	$\frac{\lvert g_1\rvert^2}{4\pi}$	$\frac{\lvert g_2\rvert^2}{4\pi}$
A	0.37	1.84
B	0.41	1.33
E	0.40	1.94

where M is a resonance mass and Γ its total width. We define the coupling constants g_i by the formula

$$\frac{g_i g_j}{4\pi} = \mathrm{i}\sqrt{s_{\mathrm{R}}} \lim_{s \to s_{\mathrm{R}}} \left[(s - s_{\mathrm{R}}) \frac{S_{ij}(s)}{\sqrt{k_i k_j}} \right]. \tag{34}$$

The product of the constants $c_i c_j$ appearing in the Breit–Wigner formula (10) is proportional to $g_i g_j$:

$$c_i c_j = \frac{[(s_{\mathrm{R}}/4 - m_i^2)(s_{\mathrm{R}}/4 - m_j^2)]^{1/4}}{2M\Gamma\sqrt{s_{\mathrm{R}}}} \frac{g_i g_j}{4\pi}. \tag{35}$$

Thus, the diagonal Breit–Wigner coupling constant corresponding to the matrix element S_{ii} given by (12) reads

$$\frac{g_{i\mathrm{BW}}^2}{4\pi} = 2M\Gamma_i \frac{\sqrt{s_{\mathrm{R}}}}{k_{iD}}, \tag{36}$$

where k_{iD} is defined by (14). One can notice that knowledge of $g_i^2/4\pi$ in the Breit–Wigner approach is equivalent to a determination of the partial width Γ_i. The two other independent quantities are M and Γ.

The coupling constants corresponding to the approximations (7) to (9) are

$$\frac{g_i^2}{4\pi} = 8\mathrm{i}\sqrt{s_{\mathrm{R}}} f_i (k_{id} + p_i). \tag{37}$$

They are complex and depend on six parameters in contrast with (36) where only three parameters appear.

Using (34) we have calculated the values of the coupling constants for the three solutions A, B and E at the two resonances $f_0(980)$ and $f_0(1400)$. They are shown in Tables 8 and 9, respectively. We can notice that the dispersion of the values of $\mid g_1 \mid^2 /4\pi$ corresponding to the $\pi\pi$ channel is the smallest one since we have mostly fitted the $\pi\pi$ data. The worst situation is in the $\sigma\sigma$ channel where there are no data available. In Table 9 we can notice that the $K\overline{K}$ coupling constants at the $f_0(1400)$ resonance are much smaller than the $\pi\pi$ coupling constants, contrary to the $f_0(980)$ resonance as seen in Table 8. Knowledge of the coupling constants is not sufficient to fully describe the S matrix elements since the coupling constants are only related to the poles. We also need the positions of the zeroes as discussed in Sect. 4.

8 Phenomenological parametrizations of multichannel amplitudes

Following our studies described in previous chapters we shall here make a proposal for a simple parametrization of

Table 9. Coupling constants of $f_0(1400)$ at the pole $---$ (in GeV^2)

Solution	$\frac{\lvert g_1\rvert^2}{4\pi}$	$\frac{\lvert g_2\rvert^2}{4\pi}$	$\frac{\lvert g_3\rvert^2}{4\pi}$
A	0.580	0.106	0.091
B	0.607	0.233	0.433
E	0.579	0.107	0.217

the multichannel amplitudes. This parametrization, based on the existence of poles and zeroes of the S matrix, has a *limited* energy range of applicability. If there is some evidence of the presence of a well separated resonance in some energy region one can use expressions (7) to (9) to describe the diagonal S matrix elements. The corresponding diagonal T matrix elements (18) read

$$T_{ii} = \frac{1}{k_i}\left(f_i - 1 + f_i\frac{k_{id}+p_i}{k_i - k_{id}}\right). \tag{38}$$

From (16) one can obtain the phase shifts and inelasticities in each channel provided that the three complex parameters (k_{id}, p_i and f_i), determined in a fit to some data, satisfy the unitarity conditions $\mid S_i \mid^2 \leq 1$ in a given energy range. The off-diagonal S matrix elements (17) can then be directly calculated as explained in [19] for the three-channel case.

The fitted parameters k_{id}, related in all channels by the energy conservation (4), provide us with the resonance energy position and its width. Other complex parameters p_i are, however, not related by (4) since they correspond to zeroes on different sheets. If we consider a three-channel fit and if the resonance appears well above the third threshold then the pole lies on sheet $---$, which means that $\mathrm{Im}\, k_{id} < 0$. The effective parameters f_i will take into account the second-order derivative corrections to the approximated Jost function as explained in Appendix B (see in particular equations (B9) to (B12)).

In Sect. 5 we have discussed the Breit–Wigner approximation. Our formula (38) can be reduced to the Breit–Wigner one if $f_i = 1$ and $\mathrm{Re}\, k_{id} \approx -\mathrm{Re}\, p_i$. Dynamically, $f_i = 1$ means that the derivatives of the Jost functions in the numerators and denominators of the S_{ii} matrix elements (like in (2)) are identically the same (see for example (B10)). The phenomenology related to the formula (38) is richer than that corresponding to the Breit–Wigner multichannel one (10) since it depends on six real parameters, while the latter one depends only on three real parameters in each channel. If one adds the so-called elastic background to the Breit–Wigner amplitude T_{ii}^{BW} then one gets the four-parameter formula

$$T_{ii} = \frac{\mathrm{e}^{2\mathrm{i}\delta_B} - 1}{2\mathrm{i}k_i} + \mathrm{e}^{2\mathrm{i}\delta_B} T_{ii}^{\mathrm{BW}}, \tag{39}$$

where δ_B is a background phase. Even introducing an inelasticity η_B to the background amplitude like

$$T_{ii} = \frac{\eta_B \mathrm{e}^{2\mathrm{i}\delta_B} - 1}{2\mathrm{i}k_i} + \eta_B \mathrm{e}^{2\mathrm{i}\delta_B} T_{ii}^{\mathrm{BW}} \tag{40}$$

Table 10. Average masses and widths of the resonances $f_0(500)$, $f_0(980)$ and $f_0(1400)$ found in our solutions A, B, E and F. Here errors represent the maximum departure from the average

Resonance	Mass (MeV)	Width (MeV)	Sheet
$f_0(500)$ or σ	523 ± 12	518 ± 14	$-++$
$f_0(980)$	991 ± 3	71 ± 14	$-++$
	1406 ± 19	160 ± 12	$---$
$f_0(1400)$	1447 ± 27	108 ± 46	$--+$

leads to a five-parameter formula. It is only when one enlarges the number of independent parameters in the T_{ij}^{BW} (10), by allowing c_i to be complex, that (40) is essentially equivalent to our approximation (38). The complex residues for broad overlapping states have already been introduced by several authors, in particular in [31]. The limitations of the Breit–Wigner formula have already been pointed out in previous sections. Here we see that knowledge of the S matrix poles is not sufficient to construct the scattering amplitudes. We must also know the positions of the nearby zeroes of the S matrix in order to describe the data with sufficient accuracy.

The case in which one encounters more than a single resonance lying near the threshold should be treated differently, especially if one wishes to study the energy range containing that threshold. Then in general more than one S matrix pole should be taken into account. In our analysis near 1400 MeV such a secondary pole appears on sheet $--+$ close to the physical region. Therefore, this pole is included in Table 10, showing the average values of the masses and widths of the scalar resonances $f_0(500)$, $f_0(980)$ and $f_0(1400)$ obtained by us. Its mass is higher and its width is smaller than those of the $---$ pole. The three states $f_0(500)$, $f_0(980)$ and $f_0(1400)$ can be regarded as the model-independent resonances since they appear in all our solutions. The positions of other far-lying poles above 3 GeV for the solutions A or B, of the pole around 1700 MeV in solution E and of the pole at 1349 MeV in solution F are strongly model dependent.

Finally, let us remark that formula (38) can be used to approximate the meson–meson transition amplitudes in different reactions where meson pairs appear. This would be the case in meson-production processes by hadrons, leptons and photons, in $\gamma\gamma$ reactions or in central pp production, in heavy-particle decays, in baryon–antibaryon annihilation, and so on.

9 Summary

We have presented two new solutions, E and F, resulting from fits to the experimental data on the $\pi\pi$ and $K\overline{K}$ phase shifts and inelasticities. Both new solutions are characterized by the existence of a $K\overline{K}$ bound state when the interchannel couplings are switched off. In the previously found solutions A and B, the $K\overline{K}$ pair remained unbound in the uncoupled case (see Table 2). In Tables 3 to 6 we

have given for each solution the set of S matrix poles lying on different sheets. Knowledge of their positions is necessary in order to evaluate the masses, widths, branching ratios and coupling constants of the scalar resonances studied here. Furthermore, we stress that not only the poles of the S matrix but also its *zeroes* play a very important role in the evaluation of the resonance parameters. All zeroes are dynamically related. Also knowledge of the pole trajectories as a function of the interchannel coupling strengths is important to find the origin of the resonances. The fact that we have obtained different solutions while fitting the experimental data is mainly due to the limited number of data and due to their limited precision. We hope, however, that this situation can be improved in the future when new data of better precision will appear and the same model is applied to a wider class of reactions. Then one should be able to get nearly model-independent information on the resonances lying sufficiently close to the physical energy axis. However, the poles lying far away from this axis will obviously be subject to some model dependence.

We have paid special attention to the phenomenological analysis of the energy region near 1400 MeV where new scalar resonances appear [1]. A simple model of the S matrix in the three channels $\pi\pi$, $K\overline{K}$ and 4π, represented by an effective $\sigma\sigma$, has been constructed ((7) to (9) and (38)). This parametrization could be used to phenomenologically represent the meson–meson amplitudes in different reactions. The model is based on our knowledge of the pole on sheet $---$, common to all three channels, and the zero which is specific for each channel. The diagonal S matrix elements depend on three complex parameters (positions of the pole and of the zero, and the strength). This is in contrast with the Breit–Wigner formalism, where only three real parameters describe the resonance amplitudes. The Breit–Wigner approach has limited applicability since it restricts too much the positions of the zeroes and thus it does not take fully into account the interchannel dynamics.

Branching ratios for different channels were defined and calculated for two- and three-channel models. We have studied the energy regions of the $f_0(980)$ and $f_0(1400)$ resonances and the region between them. We have noticed that different definitions of the branching ratios were used in the literature, which led to some confusion in the past. The result is that there are no data on the $\pi\pi$ and $K\overline{K}$ branching ratios of $f_0(980)$ and the incorrect determinations of them were no more given in the new edition of the Particle Data Tables [1].

Above the third threshold the branching ratios form a 3×3 matrix. Each row of this matrix describes three branching ratios in the particular channel, but only two of them are independent quantities (see (25)). Phenomenological information contained in such a matrix is much richer than in the Breit–Wigner approach where only three branching ratios can be used. We have studied the energy interval of 1350 MeV to 1500 MeV and found small branching ratios corresponding to the transitions from the $\pi\pi$ to $K\overline{K}$ channel and vice versa. This is in qualitative agreement with the findings of the Crystal Barrel Group [28, 29].

We have given formulae (34), (36) and (37) for the coupling constants in the three-channel model and its different approximations. Calculated values of the coupling constants in the full model are reported in Tables 8 and 9. The $f_0(980)$ couples strongly to $K\overline{K}$ and the coupling of $f_0(1400)$ is much stronger for the $\pi\pi$ channel than for the $K\overline{K}$ channel. One should point out that knowledge of the resonance mass and width and the coupling constants is not sufficient to give a good phenomenological description of the meson–meson dynamics.

We have found that a fit of the $\pi\pi$ data of [8] together with the $K\overline{K}$ phase shifts of [15] requires a $f_0(1406 \pm 19)$ on sheet $---$ and a $f_0(1447 \pm 27)$ on sheet $--+$ (see Table 9). This seems to indicate that these data are quite compatible with Crystal Barrel and other LEAR experiments which need a broad $f_0(1370)$ and a narrower $f_0(1500)$ [1]. To make a closer fit to the results obtained by these experiments one could perform a simultaneous analysis of the $\pi^- p_\uparrow \to \pi^+\pi^- n$ data and the data on $p\overline{p} \to 3\pi^0, 5\pi^0$ and other reactions. The model described by us can provide the production and scattering amplitudes of nine reactions. These amplitudes can be applied in the description of the final state interactions between particles produced in different reactions. If needed, our model of the meson–meson interactions can be extended to describe more than three coupled channels (like $\eta\eta$, $\eta\eta'$ and so on). Our model is also sufficiently flexible to accommodate scalar mesons at energies higher than 1500 MeV, like the $f_J(1710)$ (see Table 5).

In the present version of our model the mass of the third channel is introduced as a free parameter. It is possible to construct a more involved model where one smears out this mass over a rather broad range according to the observed invariant $\pi\pi$ mass distribution. Crossing symmetry constraints, if implemented, might also lead to a reduction of the number of parameters. Evidently, new measurements should be performed near different meson–meson thresholds since even at the $K\overline{K}$ threshold the present data do not allow one to obtain the $f_0(980)$ branching ratios. New data would help us to test different models of intermeson interactions. This will lead to a more profound knowledge of the structure of the scalar mesons.

Acknowledgements. We would like to thank Krzysztof Rybicki for very useful discussions. This work has been performed in the framework of the IN2P3–Polish laboratories Convention (project No. 93-71).

Appendix A

Here we give the full formula for the Jost function $D \equiv D(k_1, k_2, k_3)$ of our unitary model, built to describe the three channels $\pi\pi$, $K\overline{K}$ and the effective $2\pi2\pi$ ($\sigma\sigma$). Using the same notation as in [7] we have

$$D = d_0 D_0 + \lambda_{00} I_{01} D_1 - \lambda_{02} I_{22} D_2 - \lambda_{03} I_{33} D_3, \quad \text{(A1)}$$

where

$$d_i = 1 - \lambda_{ii} I_{ii}, \qquad i = 0, 1, 2, 3, \tag{A2}$$

$$D_0 = \widetilde{D_0} - \lambda_{02} I_{01} I_{22} C_2 - \lambda_{03} I_{01} I_{33} C_3, \tag{A3}$$

$$C_2 = \lambda_{12} + I_{33}(\lambda_{13}\lambda_{23} - \lambda_{12}\lambda_{33}), \tag{A4}$$

$$C_3 = \lambda_{13} + I_{22}(\lambda_{12}\lambda_{23} - \lambda_{13}\lambda_{22}), \tag{A5}$$

$$\begin{aligned}\widetilde{D_0} = {} & d_1 d_2 d_3 - 2\lambda_{12}\lambda_{13}\lambda_{23} I_{11} I_{22} I_{33} \\ & - \lambda_{13}^2 I_{11} I_{33} d_2 - \lambda_{12}^2 I_{11} I_{22} d_3 - \lambda_{23}^2 I_{22} I_{33} d_1,\end{aligned} \tag{A6}$$

$$\begin{aligned}D_1 = {} & -I_{01} d_2 C_1 + \lambda_{23}(\lambda_{11}\lambda_{23} - \lambda_{12}\lambda_{13}) I_{01} I_{22} I_{33} \\ & - (\lambda_{02} I_{00} + \lambda_{12} I_{01}) I_{22} C_2 - \lambda_{03} I_{00} I_{33} C_3,\end{aligned} \tag{A7}$$

$$C_1 = \lambda_{11} + I_{33}(\lambda_{13}^2 - \lambda_{11}\lambda_{33}), \tag{A8}$$

$$\begin{aligned}D_i = {} & \lambda_{0i}\{I_{01}^2[\lambda_{11} + I_{jj}(\lambda_{1j}^2 - \lambda_{11}\lambda_{jj})] \\ & + I_{00}[d_1 d_j - \lambda_{1j}^2 I_{11} I_{jj}]\} \\ & + \lambda_{0j} I_{jj}[\lambda_{23} I_{00} d_1 + \lambda_{11}\lambda_{23} I_{01}^2 \\ & + \lambda_{12}\lambda_{13}(I_{00} I_{11} - I_{01}^2)] \\ & + \lambda_{1i} I_{01} d_j + \lambda_{1j}\lambda_{23} I_{01} I_{jj},\end{aligned} \tag{A9}$$

where $i = 2, 3$; $j = 3$ if $i = 2$ and $j = 2$ if $i = 3$.

Appendix B

We derive an approximated formula for the pion–pion S matrix element given by (2). First, let us make an expansion of the Jost function in the denominator of S_{11} near its zero on sheet $---$ at $\boldsymbol{k}_d = (k_{1d}, k_{2d}, k_{3d})$:

$$D(\boldsymbol{k}) \equiv D(k_1, k_2, k_3) \approx (k_1 - k_{1d}) d_1 + \frac{1}{2}(k_1 - k_{1d})^2 s_1. \tag{B1}$$

Here

$$\begin{aligned}d_1 = {} & \left[\frac{\partial D(k_1, k_2, k_3)}{\partial k_1} + \frac{k_{1d}}{k_{2d}} \frac{\partial D(k_1, k_2, k_3)}{\partial k_2}\right. \\ & \left. + \frac{k_{1d}}{k_{3d}} \frac{\partial D(k_1, k_2, k_3)}{\partial k_3}\right]_{\boldsymbol{k} = \boldsymbol{k}_d}\end{aligned} \tag{B2}$$

and

$$\begin{aligned}s_1 = {} & \left[\frac{\partial^2 D(k_1, k_2, k_3)}{\partial k_1^2}\right. \\ & + \frac{{k_{1d}}^2}{{k_{2d}}^2} \frac{\partial^2 D(k_1, k_2, k_3)}{\partial k_2^2} + \frac{{k_{1d}}^2}{{k_{3d}}^2} \frac{\partial^2 D(k_1, k_2, k_3)}{\partial k_3^2} \\ & \left. + 2\frac{k_{1d}}{k_{2d}} \frac{\partial^2 D}{\partial k_1 k_2} + 2\frac{k_{1d}}{k_{3d}} \frac{\partial^2 D}{\partial k_1 k_3} + 2\frac{{k_{1d}}^2}{k_{2d} k_{3d}} \frac{\partial^2 D}{\partial k_2 k_3}\right]_{\boldsymbol{k} = \boldsymbol{k}_d}\end{aligned} \tag{B3}$$

In (B2) and (B3) we have used the relations

$$k_2 - k_{2d} \approx (k_1 - k_{1d}) \frac{k_{1d}}{k_{2d}}, \tag{B4}$$

$$k_3 - k_{3d} \approx (k_1 - k_{1d}) \frac{k_{1d}}{k_{3d}}, \tag{B5}$$

which follow from energy conservation (4). Similarly, we make a power expansion of the Jost function in the numerator of S_{11}. Let us denote by $\boldsymbol{k}_n = (k_{1n}, k_{2n}, k_{3n})$ a zero of $D(k_1, k_2, k_3)$ on sheet $-++$:

$$D(k_{1n}, k_{2n}, k_{3n}) = 0. \tag{B6}$$

Then using (1) we expand

$$D(-k_1, k_2, k_3) \approx (k_1 - {k_{1n}}^*) c_1 + \frac{1}{2}(k_1 - {k_{1n}}^*)^2 t_1, \tag{B7}$$

where

$$\begin{aligned}c_1 = {} & \left[-\frac{\partial D(-k_1, k_2, k_3)}{\partial k_1} - \frac{k_{1n}}{k_{2n}} \frac{\partial D(-k_1, k_2, k_3)}{\partial k_2}\right. \\ & \left. - \frac{k_{1n}}{k_{3n}} \frac{\partial D(-k_1, k_2, k_3)}{\partial k_3}\right]_{\boldsymbol{k} = -\boldsymbol{k}_n^*}\end{aligned} \tag{B8}$$

and t_1 is given by an equation similar to that for s_1 in (B3). With the help of (B1) and (B7) the pion–pion S matrix element reads

$$S_{11} \approx \frac{k_1 - k_{1n}^*}{k_1 - k_{1d}} f_1, \tag{B9}$$

where

$$f_1 = \frac{c_1}{d_1} F(k_1), \tag{B10}$$

$$F(k_1) = \frac{1 + \frac{1}{2}\frac{t_1}{c_1}(k_1 - {k_{1n}}^*)}{1 + \frac{1}{2}\frac{s_1}{d_1}(k_1 - k_{1d})}. \tag{B11}$$

The function $F(k_1)$ can further be approximated by a constant if we limit ourselves to values k_1 close to $\mathrm{Re}\, k_{1d}$ in the denominator of $F(k_1)$ and close to $\mathrm{Re}\, k_{1n}$ in its numerator:

$$F(k_1) \approx \frac{1 + \frac{1}{2}\frac{t_1}{c_1} \mathrm{i}\mathrm{Im}\, k_{1n}}{1 - \frac{1}{2}\frac{s_1}{d_1} \mathrm{i}\mathrm{Im}\, k_{1d}}. \tag{B12}$$

Similar expressions can be derived for the diagonal $K\overline{K}$ and $\sigma\sigma$ S matrix elements.

References

1. Particle Data Group, C. Caso et al., Europ. Phys. J. C **3**, 1 (1998)
2. **Proceedings of the Hadron Spectroscopy Conference**, Upton, NY, August 1997, edited by S.-U. Chung, H.J. Willutzki, American Institute of Physics, Woodbury, New York (1998)
3. F.E. Close, G.R. Farrar, Z. Li, Phys. Rev. D **55**, 5749 (1997)
4. W. Lee, D. Weingarten, Nucl. Phys. B **63** A–C (Proc. Supl.), 194 (1998)
5. C. Michael, see [2] p. 657.
6. F.E. Close, Nucl. Phys. B **63** A–C (Proc. Supl.), 28 (1998)
7. R. Kamiński, L. Leśniak, B. Loiseau, Phys. Lett. B **413**, 130 (1997)
8. R. Kamiński, L. Leśniak, K. Rybicki, Z. Phys. C **74**, 79 (1997)

9. R. Kamiński, L. Leśniak, J.-P. Maillet, Phys. Rev. D **50**, 3145 (1994)
10. A. Abele et al., Phys. Lett. B **380**, 453 (1996)
11. N.N. Achasov, G.N. Shestakov, Phys. Rev. D **58**, 054011 (1998)
12. L. Rosselet et al., Phys. Rev. D **15**, 574 (1977)
13. A.A. Belkov et al., Pisma Zh. Eksp. Teor. Fiz. **29**, 652 (1979)
14. V. Srinivasan et al., Phys. Rev. D **12**, 681 (1975)
15. D. Cohen et al., Phys. Rev. D **22**, 2595 (1980)
16. G. Grayer et al., Nucl. Phys. B **75**, 189 (1974)
17. H. Becker et al., Nucl. Phys. B **151**, 46 (1979)
18. W.M. Kloet, B. Loiseau, Eur. Phys. J. A **1**, 337 (1998).
19. L. Leśniak, Acta Phys. Pol. B **27**, 1835 (1996)
20. Particle Data Group, Phys. Rev. D **45**, part II (1992); Particle Data Group, Phys. Rev. D **50**, part I (1994)
21. P.F. Loverre et al., Z. Phys. C **6**, 187 (1980).
22. W. Wetzel et al., Nucl. Phys. B **115**, 208 (1976)
23. N.M. Cason et al., Phys. Rev. **41**, 271 (1978)
24. D. Morgan, M.R. Pennington, Phys. Rev. D **48**, 1185 (1993)
25. D.V. Bugg, A.V. Sarantsev, B.S. Zou, Nucl. Phys. B **471**, 59 (1996)
26. F. Cannata, J.-P. Dedonder, L. Leśniak, Phys. Lett. B **207**, 115 (1988)
27. L. Goerlich et al. (CERN–Cracow–Munich Collaboration), Nucl. Phys. B **174**, 16 (1980)
28. C. Amsler, Rev. Mod. Phys. **70**, 1293 (1998)
29. A. Abele et al., Phys. Rev. D **57**, 3860 (1998)
30. A. Abele et al., Nucl. Phys. A **609**, 562 (1996)
31. K.L. Au, D. Morgan, M.R. Pennington, Phys. Rev. D **35**, 1633 (1987)